Prepared for submission to JINST

Time performance of USTC-IME LGAD under synchrotron light source focused X-ray

T.A. Wang,[a] D. Zhang,[a] Z. Liang,[a] Y.W. Liu,[a] C.Z. Li,[b] J.Q. Luo,[c] Y. Nie,[a] T.S. Yue[a]

[a] *Department of Modern Physics, University of Science and Technology of China, Hefei 230026, China*

[b] *College of science, National University of Defense Technology, Changsha 410073, China*

[c] *Key Laboratory of Nuclear Physics and Ion-beam Application (MOE), Institute of Modern Physics, Fudan University, Shanghai 200433, China*

E-mail: yanwen@ustc.edu.cn

Abstract: The time performance of Low Gain Avalanche Diodes (LGADs), designed by the University of Science and Technology of China (USTC) and fabricated by the Institute of Microelectronics of Chinese Academy of Sciences (IME), was characterized at the Shanghai Synchrotron Radiation Facility (SSRF). The experiment was conducted at the BL16B1 beamline, which delivers a focused X-ray beam with a diameter of 500 µm, a repetition period of 2 ns, and a photon energy of 10 keV. Using a fast oscilloscope, waveforms containing continuous signal pulses were recorded within a 50 ns time window. The LGAD under test successfully resolved the 2 ns period of the SSRF. To mitigate pile-up effects and extract pulse-by-pulse information from the acquired waveforms, a waveform-level global template fitting method was employed. The time resolution was then estimated using a combined profile likelihood approach, yielding a value of 126.6 ps. The effect of random photon absorption depth on the time resolution of LGADs was studied through dedicated simulations.

Keywords: Particle tracking detectors (Solid-state detectors); Timing detectors; X-ray detectors

ArXiv ePrint: 1234.56789

arXiv:2609.00972v1 [physics.ins-det] 1 Sep 2026

[1] Corresponding author.

Contents

1 Introduction **1**

2 Devices tested **2**

3 Experimental setup at SSRF **3**

4 Data analysis **4**
- 4.1 Extraction of the repetition period 5
- 4.2 Global template fit for fine time analysis 5

5 Simulation for a better understanding **10**

6 Conclusions **11**

1 Introduction

The Low Gain Avalanche Diode (LGAD) is a type of silicon sensor characterized by excellent time resolution, fast rising time, short dead time, and high radiation tolerance [1, 2]. In recent years, it has garnered increasing attention in the field of experimental particle physics. Both the ATLAS and CMS experiments at the Large Hadron Collider (LHC) have adopted LGADs for their upgrade projects [3, 4]. Designed by the University of Science and Technology of China (USTC) and fabricated by the Institute of Microelectronics of Chinese Academy of Sciences (IME), the USTC-IME LGADs have been developed for the ATLAS High Granularity Timing Detector (HGTD) project [5, 6]. Building on this success, the team is exploring additional scientific and technological applications for these sensors.

Owing to a highly doped gain layer, located a few micrometers beneath the charge collection electrode, LGADs provide inherent gain. This enables X-rays to generate sufficient charge within a thin silicon layer for readout by front-end electronics. To investigate this potential, several research groups have begun studying the response of LGADs to X-rays [7–10]. LGAD sensors from Hamamatsu Photonics (HPK), Brookhaven National Laboratory (BNL), and Fondazione Bruno Kessler (FBK) were tested at the Stanford Synchrotron Radiation Lightsource (SSRL). The energy resolution and timing performance of these LGADs were characterized as functions of bias voltage and incident photon energy. All tested LGAD sensors successfully resolved the 2.1 ns repetition period of the SSRL. For 35 keV X-ray beams, the HPK 3.1 LGAD at a bias voltage of 150 V and the BNL LGAD with a thickness of 20 µm at a bias voltage of 50 V achieved the best energy resolution of 6%. The BNL LGAD showed the best time resolution of 65 ps at a bias voltage of 100 V [8]. In this work, the USTC team has also characterized the time performance of USTC-IME LGADs for hard X-rays at the Shanghai Synchrotron Radiation Facility (SSRF) [11]. The SSRF has a single-pulse jitter of 28.3 ps and a repetition period of 2 ns [12]. The tested sensors were able to resolve

the repetition period. Moreover, the jitter of the source is sufficiently small to allow for an accurate evaluation of the sensor time resolution. Earlier studies applied a smoothing method to correct the baseline fluctuation in waveforms, but analyzed only signals that were well separated in time [8–10]. In this work, a waveform-level global template fit was employed to extract information of all signal pulses including those affected by precedent pulses, referred to as pile-up effects hereafter.

The tested devices are introduced in section 2 and detailed information regarding the beamline station and the experimental setup is presented in section 3. Two analysis methods were employed to characterize time performance. Section 4.1 presents the extraction the repetition period of the SSRF. Section 4.2 describes the fine analysis of the time resolution using the global template fit. To better understand the time resolution, a simulation combining Allpix Squared and TCAD Sentaurus was performed to investigate the signal generation process of X-rays in LGADs [13, 14], as detailed in Section 5.

2 Devices tested

Two single-pad sensors from the USTC-IME version 2.1 batch were tested [15], each with an active thickness of 50 µm. To increase the detection efficiency, most of the aluminum beneath the passivation layer was removed, creating a large entering window on the active region surface. Calibrated with a beta source at room temperature (26 ℃), both sensors exhibited time resolutions of 39.6 ps. One sensor was used as the device under test (DUT), while the other served as the trigger (denoted as reference). Their I-V curves at 20 ℃ are illustrated in figure 1. Each sensor was wire-bonded to an ultra-fast low-noise preamplifier board for readout [16]. Because the amplifier board introduces additional impedance, the effective bias voltage applied to the the sensor is lower than the voltage applied to the board. In this study, the applied voltage was set to 180 V for both boards, corresponding to a total current of 100 nA, which, based on prior experience, indicates that the sensors were operating under nominal conditions. Photographs of the sensor and the board are shown in figure 2.

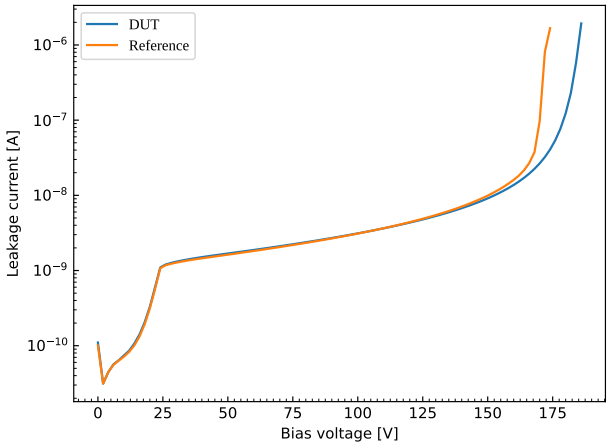

Figure 1: I-V curves of the tested sensors

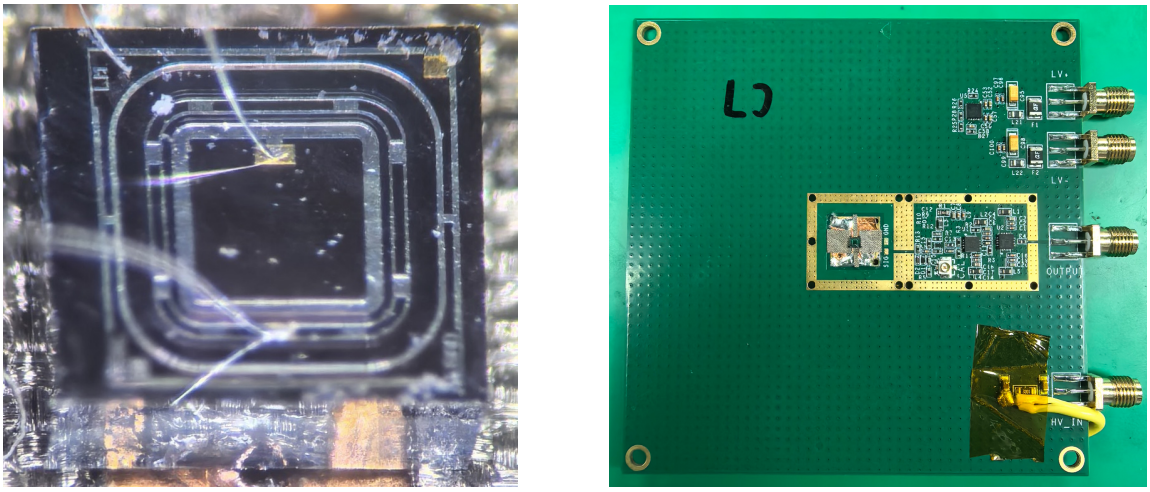

(a) (b)

Figure 2: (a) Photograph of a USTC-IME version 2.1 LGAD sensor, showing a window on the surface of the sensitive area. (b) Photograph of the ultra-fast low-noise preamplifier board.

3 Experimental setup at SSRF

The experiment was conducted at the BL16B1 beamline station of the SSRF [17]. The beamline delivers a fixed photon energy of 10 keV, and each spill contains approximately 400 photons. The beam is focused to a spot size of about 500 µm in diameter, which is comparable to the sensitive region of the tested sensors.

The experimental setup is shown in figure 3. The DUT and the reference sensors, along with their preamplifier boards, were mounted on an optical motion stage capable of fine alignment in three directions. Behind the fixture, a gas ionization chamber and a Pilatus2M detector, provided by the beamline station, were used to measure the beam intensity. An aluminum shield was placed in front of the sensors to attenuate the photon beam. Signals were recorded using an oscilloscope with a bandwidth of 4 GHz and a sampling rate of 40 GS/s. Upon each trigger initiated by the reference sensor, the osilloscope digitize and record the data for a duration of 50 ns. Two Keithley 2470 high-voltage sourcemeters separately supplied the bias voltages for the DUT and the reference, while one Keithley 2231A-30-3 triple-channel DC power supply provided low voltage to power the boards. The oscilloscope and the sourcemeters were controlled by a laptop in the control room.

The photon energy of 10 keV is very close to the energy deposited by a minimum ionizing particle (MIP) in a 50-µm silicon layer. We aimed to ensure that only one photon could be detected per spill, in order to study the difference in time performance of USTC-IME LGADs when detecting X-rays and MIPs. After numerous attempts, according to the average signal amplitude and the trigger rate, appropriate waveforms were observed with an 1-mm-thick aluminum shield. Figure 4a shows a representative waveform in this situation. With a thicker shield, the average signal amplitude remained unchanged, while both the number of pulses in a waveform and the trigger rate decreased, indicating that no more than one photon could pass through the shield within a time window of 50 ns. Therefore, the shield thickness of 1 mm was adopted for most of the experiment to acquire the

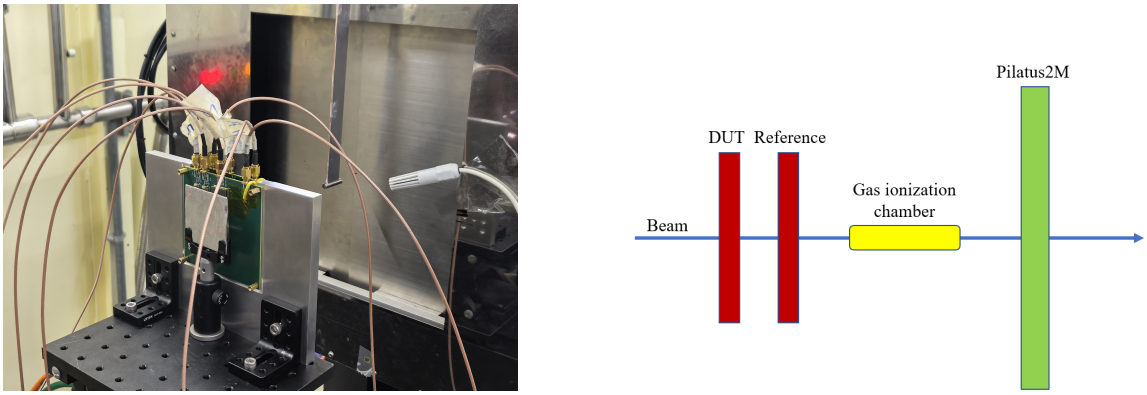

(a) (b)

Figure 3: Experimental setup at the BL16B1 beamline station of the SSRF. The beam is incident from the left, with the DUT positioned in front of the reference.

primary data set. Additional data sets were also collected using thicker shields. For example, with a 2.2-mm-thick shield, nearly all acquired waveforms contained only one single pulse, as shown in figure 4b. These data can be used to study the shape of the X-ray signal in USTC-IME LGADs, which will be discussed in section 4.2.

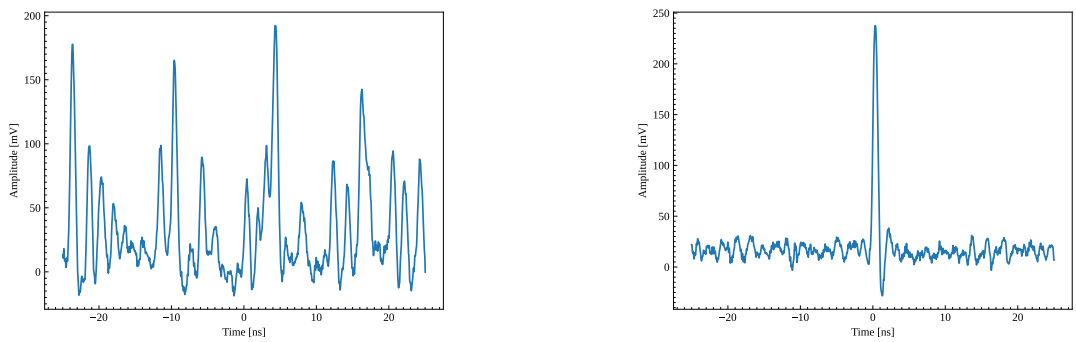

(a) (b)

Figure 4: (a) Representative waveform with a 1-mm-thick shield. (b) Representative waveform with a 2.2-mm-thick shield.

4 Data analysis

Since the 2 ns repetition period of the SSRF is comparable to the response time of our detection system, pile-up effects occur between adjacent signal pulses in the DUT waveforms, as illustrated in figure 4a. This phenomenon complicates the establishment of a stable baseline, thereby affecting the accurate determination of signal amplitudes and time of arrival (TOA) via constant fraction discrimination (CFD). In this section, after having obtained the repetition period of the light

source, we performed a waveform-level global template fit on the periodic multi-pulse waveforms to effectively address the pile-up problem.

4.1 Extraction of the repetition period

Because of the shielding effect of the DUT, the reference sensor predominantly captured single-pulse signals with stable baselines. Prior to data taking, waveforms of the DUT and the reference sensor were shifted to overlap on the oscilloscope, therefore, the baseline of the reference sensor was adopted as an estimate for that of the DUT. For each coincidence event, the average voltage sample over the first 5 ns segment of the waveform of the reference detector was selected as the estimated baseline. This estimated baseline was subsequently subtracted from the DUT waveform before determining the TOA. This approach provides only a rough estimation and is insufficient for analyzing time resolution at the sub-nanosecond level. Therefore, it was used solely to extract the repetition period of the SSRF. The TOA of each pulse with respect to the TOA of the first pulse were computed. These waveforms were captured from the DUT within a time window of 50 ns, wherein the continuous signal pulses corresponded to successive beam spills. These TOA with respect to the first pulse represent the time intervals between beam spills. Figure 5a shows the distribution of these differences, where only signal pulses with amplitudes exceeding 100 mV are considered, as the trigger threshold was set to 100 mV. The distribution exhibits multiple peaks, each of which was fitted with a Gaussian function to obtain its center. The resulting peak centers demonstrate good linearity, with a slope of 2 ns, as shown in Figure 5b. This slope corresponds exactly to the repetition period of the SSRF, indicating that LGADs are suitable for diagnostics of synchrotron radiation X-rays.

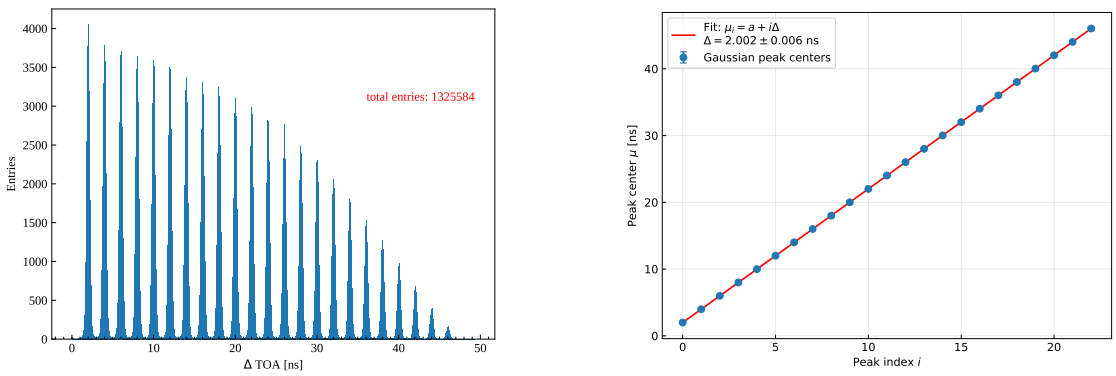

(a) (b)

Figure 5: (a) Distribution of ΔTOA. (b) Fitted peak centers of figure 5a and their linear fit result.

4.2 Global template fit for fine time analysis

In the previous study conducted at the SSRL, it was observed that the time resolution of LGADs is significantly worse when detecting X-rays compared to detecting MIPs [8]. This degradation is primarily attributed to the large variation in the depth at which photons are absorbed. Unlike MIPs,

which generate electron-hole pairs along their entire trajectories, incident photons are typically absorbed at a highly localized region. Consequently, the generated charge carriers must drift varying distance to reach the gain layer. The simulation predicts that in a 50-µm-thick LGAD sensor, the maximum difference in drift time can exceed 500 ps. The details of the simulation will be described in section 5. This variation results in a fluctuating delay time of the signal. Therefore, this delay time is the key to understand time performance of LGADs in detecting X-rays.

Since all signal pulses originate from the same physical process—namely, the deposition of a 10 keV photon in silicon, the expected pulse shape should be consistent, which can be characterized by a common signal template. This property enables a multi-peak fitting approach to extract the information of individual pulses, mitigating the pile-up effects that distorts the rising edge of the pulses. Such a methodology has been widely adopted in high energy physics, particularly for improving energy resolution [18, 19]. In this work, we adapt this technique for fine time analysis. The fitting formula for waveform w is given by Equation (4.1):

$$\begin{gathered} y_{iw} = \sum_{k \in L_w} A_{kw} h(t_{iw} - \tau_{kw}) + \sum_{j \in S_w} A_{jw} h(t_{iw} - \tau_{jw}) + b_w(t_{iw}) \,, \\ \tau_{kw} = kT + \delta t_{kw} + \Delta t_w, \quad \tau_{jw} = jT + \delta t_{jw} + \Delta t_w, \quad L_w, S_w \subseteq [-12, -11, \ldots, 12, 13] \,, \\ b_w(t_{iw}) = a_w + c_w t_{iw} \,, \end{gathered} \tag{4.1}$$

where y_{iw} is the voltage sample at time t_{iw}; L_w and S_w are the sets of serial numbers corresponding to large and small pulses according to the 100 mV threshold, which is the trigger level; k and j are the indices determined by the relative positions of the respective pulses on the waveform; A_{kw} and A_{jw} are the amplitudes of the k-th and j-th pulses, respectively; $h(t)$ is the normalized signal template; τ_{kw} and τ_{jw} are the reference time of the k-th and j-th pulses corresponding to t = 0 for $h(t)$; T is the repetition period of the SSRF of 2 ns; δt_{kw} and δt_{jw} are the concerned random delay time; Δt_w is a waveform-level global time shift, from the fluctuation of the trigger signal with respect to the beam clock; and $b_w(t)$ is a linear term accounting for potential noise.

The determination of τ_{kw} and τ_{jw} was the most critical step in the fitting procedure. In principle, they should be governed primarily by T. However, the BL16B1 beamline station does not provide a synchronous clock signal, so the DUT had to be triggered by the reference sensor. Therefore, the trigger time did not necessarily match the repetition period of 2 ns. Consequently, the waveform-level global time shift Δt_w must be incorporated into τ_{kw} and τ_{jw} to achieve proper alignment in time. In addition, the random delay time δt_{kw} and δt_{jw} must be taken into account.

Fitting δt_{kw} and δt_{jw} for every pulse individually, together with Δt_w, would introduce an excessively large number of free parameters and increase the complexity of the fit. To address this issue, a simplified treatment was adopted. Δt_w was not treated as a floating parameter in the fit; instead, it was determined by scanning within a range of ±0.1 ns around the TOA of the pulse closest to the trigger time, with a step size of 2 ps, so as to minimize the residual sum of squares (RSS). The TOA was shifted into the range of -1 ns to 1 ns after taking modulo 2 ns, thereby ensuring that the time shift does not exceed half a period plus 0.1 ns. Figure 6 represents the effect of the Δt_w scan. Furthermore, given that the fitting accuracy for small pulses is significantly worse than that for large ones, these two groups were optimized separately. For small pulses and regions without signal pulses, δt_{jw} was not considered, and τ_{jw} was determined solely from T and Δt_w. In contrast, for large pulses, τ_{kw} was constructed using only T and the fitted δt_{kw}, without explicitly incorporating

Δt_w into the expression. This was to prevent the known Δt_w from dominating the RSS minimization and thereby degrading the fit quality. It should be noted that δt_{kw} obtained in this manner inherently includes Δt_w, and thus the time resolution derived from it also incorporates the contribution from waveform-to-waveform variations in the time shift. This uncertainty ultimately originates from the lack of a synchronous clock signal. To facilitate the fitting, linear approximation in terms of δt_{kw} was applied for the signal template. The resulting fitting expression is given by Equation (4.2).

$$y_{iw} \approx \sum_{k \in L_w} A_{kw} [h(t_{iw} - kT) - \dot{h}(t_{iw} - kT)\delta t_{kw}] + \sum_{j \in S_w} A_{jw} h(t_{iw} - jT - \Delta t_w) + a_w + c_w t_{iw} \,, \quad (4.2)$$

where $h(t)$ and $\dot{h}(t)$ were set to zero outside the time window from -2 ns to 5 ns.

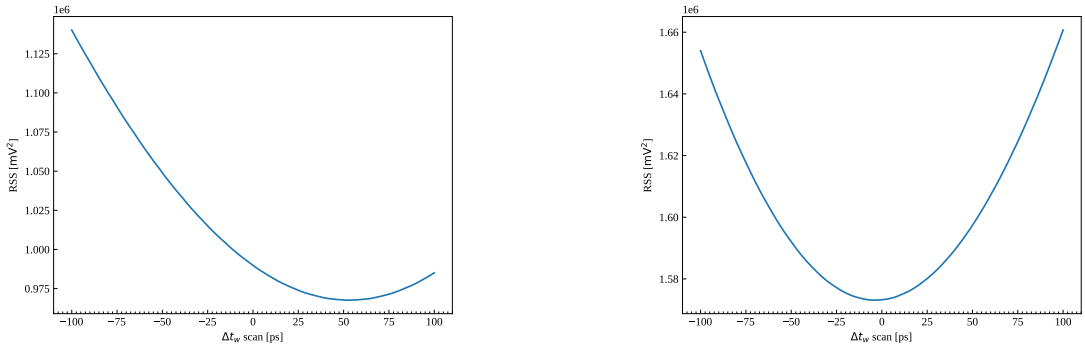

(a) (b)

Figure 6: Effect of the Δt_w scan on two representative waveforms. The Δt_w was selected to minimize the RSS.

The signal template was derived from a set of waveforms acquired with a 2.2-mm-thick aluminum shield, as described in section 3. After excluding waveforms characterized by excessive noise or containing more than one pulses, a total of 8,027 waveforms were retained for analysis. The rising time (from 10% to 90% of the rising edge) of these pulses was evaluated, yielding a root mean square (RMS) value of 86 ps, as illustrated in figure 7. The average waveform was adopted as the template. The construction procedure was as follows: first, the 50% CFD TOA of each pulse was shifted to t = 0 for temporal alignment; then, a unified time grid spanning from –2 ns to 5 ns with a step of 0.01 ns was selected to cover the entire pulse; and their amplitudes were normalized to unity; finally, the template was obtained by averaging the normalized pulses, as shown in figure 8.

Figure 9 presents a representative fitting result, showing that the large pulses are well characterized. After excluding waveforms with excessive RSS as shown in figure 10 and pulses with signal amplitude below 100 mV or an excessively large valley, the distribution of the fitted δt_{kw} values is presented in figure 11. A direct Gaussian fit proves suboptimal, with the fitted mean deviating from 0. This is primarily attributed to the waveform-to-waveform variations in Δt_w. An attempt is made to eliminate this effect as follows.

The quantity δt_{kw} should follow a certain distribution, of which the RMS is the time resolution of the LGAD in detecting the X-ray. In the approach above, the mean values of δt_{kw} per each pulse is shifted by the influence of imprecise Δt_w, but the δt_{kw} in each waveform and each pulse

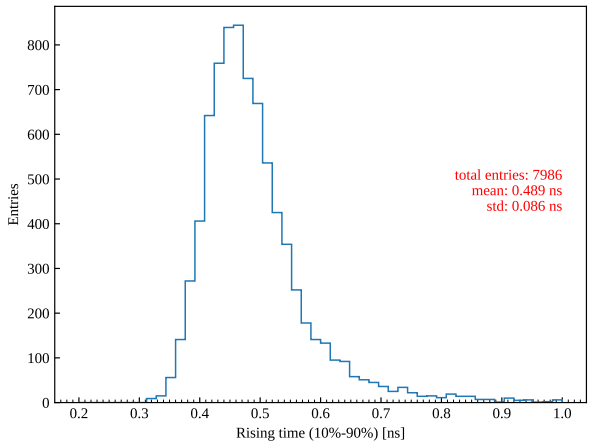

Figure 7: Distribution of the rising time (from 10% to 90% of the rising edge) of pulses used to obtain the signal template.

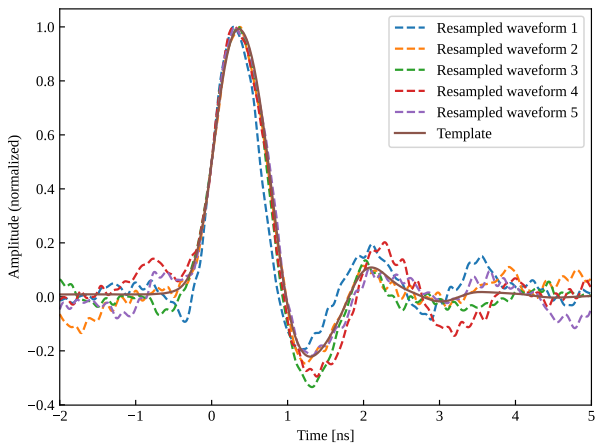

Figure 8: Signal template and some resampled waveforms.

should share a common RMS, denoted as σ hereafter. A combined profile likelihood approach is employed to estimate the common time resolution σ [20], after the same data cleaning process. For each waveform w, the mean μ_w was treated as a nuisance parameter and profiled out by substituting its maximum likelihood estimate $\hat{\mu}_w = \bar{\delta t}_w$, where $\bar{\delta t}_w$ is the mean of δt_{kw} within waveform w. The resulting profiled negative log-likelihood for each waveform is:

$$\mathrm{NLL}_w(\sigma) = n_w \ln(\sigma) + \frac{1}{2\sigma^2} \sum_{k \in L_w} (\delta t_{kw} - \bar{\delta t}_w)^2, \tag{4.3}$$

where n_w is the number of large pulses in waveform w.The combined profile likelihood was obtained

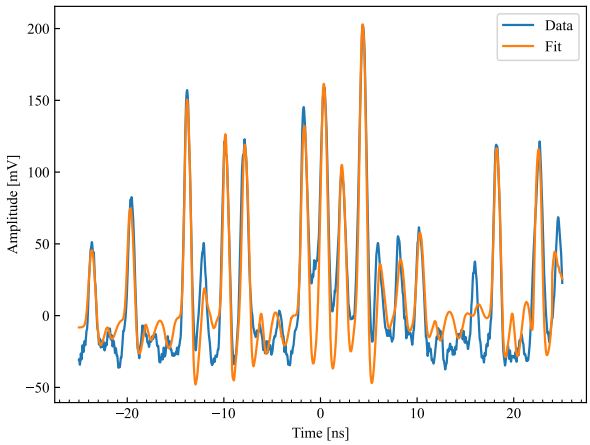

Figure 9: Representative fitting result.

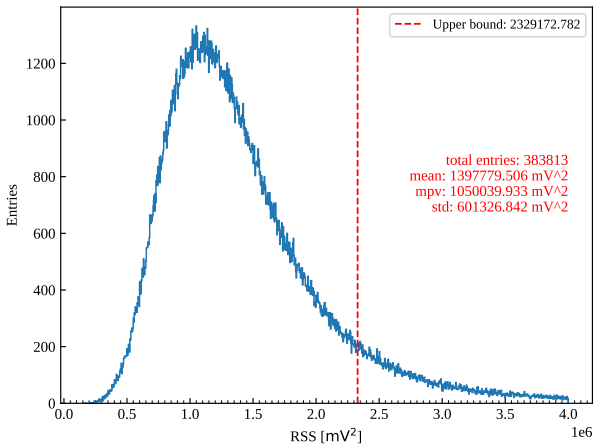

Figure 10: Distribution of the RSS. The cut is determined by the median plus 1.5 times the interquartile range.

by summing over all waveforms:

$$\mathrm{NLL}_{\mathrm{total}}(\sigma) = \sum_{w=1}^{W} \mathrm{NLL}_w(\sigma), \tag{4.4}$$

where W is the number of waveforms. The maximum likelihood estimate $\hat{\sigma}$ minimizes $\mathrm{NLL}_{\mathrm{total}}$, and the 68% confidence interval was derived from $\Delta\mathrm{NLL} = 0.5$, following Wilks' theorem [21].

A scan of the cut threshold on n_w was performed. Figure 12 presents the resulting $\hat{\sigma}$ and the number of surviving waveforms W as functions of the cut threshold. A monotonic increase in $\hat{\sigma}$ was observed, from 121.3 ps at $n_w \geq 2$ to 135.8 ps at $n_w \geq 12$. These estimated time resolutions are significantly larger than the 39.6 ps obtained when detecting MIPs. Excluding

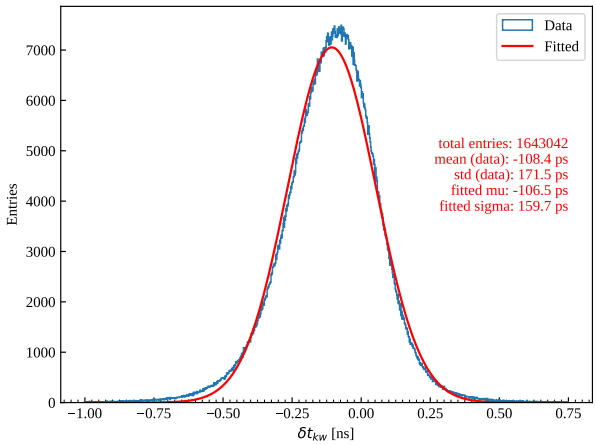

Figure 11: Distribution and Gaussian fit of δt_{kw}.

thresholds where the statistical uncertainty exceeds ±1 ps (i.e., $n_w \geq 10$), the range narrows to 121.3–130.2 ps. A cut threshold of $n_w \geq 6$ was chosen to balance statistical precision and systematic stability, yielding $\hat{\sigma} = 126.6^{+0.06}_{-0.18}$ ps, with a systematic uncertainty of ±4.4 ps (half of the observed range after excluding threshold ≥ 10) to cover the variation. The final result is: $\sigma = 126.6^{+0.06}_{-0.18}$ (stat.) ± 4.4 (syst.) ps.

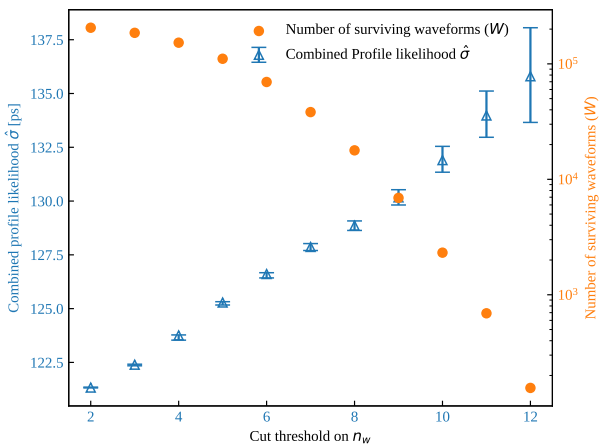

Figure 12: The resulting $\hat{\sigma}$ and the number of surviving waveforms W as functions of the cut threshold on n_w.

5 Simulation for a better understanding

To better understand the degradation in time resolution, we carried out simulations using TCAD Sentaurus and Allpix Squared. TCAD Sentaurus was employed to compute the electric field

distribution within the LGAD sensor with a bias voltage of 180 V, following the fabrication process described in [15]. Allpix Squared was utilized to simulate photon absorption and charge carrier transport within the LGAD sensor. In the simulation, the active region consists of a 50-µm-thick silicon layer, topped with a 3-µm-thick silicon dioxide layer. On the backside, a 300-µm-thick silicon substrate and a 1-µm-thick aluminum electrode were included. The photon source was configured as a single-photon beam with a fixed energy of 10 keV, focused to a spot size of approximately 500 µm in diameter, pointing to the surface of the sensor. The simulation was performed at a temperature of 28 ℃ in an air environment. All the setup was consistent with the experimental conditions. Charge carrier multiplication was intentionally disabled, as this study focuses on the charge transport dynamics prior to carriers reaching the gain layer.

The minimum time required for generated electrons to reach the gain layer was studied with respect to the injection time, which corresponds to the delay of the signal onset. Figure 13a presents the distribution of this delay, with an RMS of 150.8 ps. Figure 13b illustrates the correlation between the minimum drift time and the absorption position of the photons. Although this spread is higher than the time resolution of 126.6 ps obtained in the experiment, it shows clearly that the variation in the drift time due to localized ionization region of the X-ray photons dominate the time resolution.

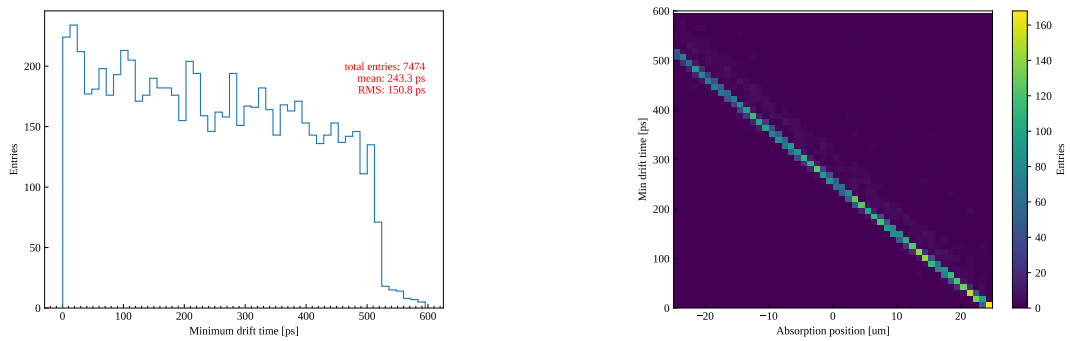

(a) (b)

Figure 13: (a) Distribution of the minimum drift time of electrons in the simulation. (b) Correlation between the minimum drift time and the absorption position of the photons obtained from simulation. The top of the active region was set at 25 um.

6 Conclusions

The time performance of a USTC-IME version 2.1 LGAD under 10 keV synchrotron focused X-rays was studied at the SSRF. The tested device successfully resolved the 2 ns repetition period of the SSRF, indicating that LGADs are capable of diagnostics for synchrotron radiation X-rays. Previous studies have shown that the time resolution of LGADs is significantly worse when detecting X-rays compared to detecting MIPs. This has been explained by the large variation of the drift lengths of the charge carriers. In this work, a global template fit was employed to extract this delay time from each individual signal pulse in multi-pulse waveforms, thereby overcoming the influence of pileup.

Then a combined profile likelihood approach was utilized to estimate the σ of this delay time. The obtained time resolution was 126.6 ps, which, as expected, is significantly worse than that for MIP detection (39.6 ps). A simulation using TCAD Sentaurus and Allpix Squared was performed to study the process by which X-rays generate signals in LGADs. The variation of the delay time was estimated to be 150.8 ps, which is consistent with the explanation.

Acknowledgments

This work is partially supported by National Natural Science Foundation of China (grant No.12535012 and No.W2443005). The authors would like to thank staff of the BL16B1 beamline of the Shanghai Synchrotron Radiation Facility (SSRF) for their experimental support.

References

[1] G. Pellegrini, P. Fernández-Martínez, M. Baselga, et al., *Technology developments and first measurements of Low Gain Avalanche Detectors (LGAD) for high energy physics applications*, *Nucl. Instrum. Methods A* **765** (2014) 12-16.

[2] H.F.-W. Sadrozinski, A. Anker, J. Chen, et al., *Ultra-fast silicon detector (UFSD)*, *Nucl. Instrum. Methods A* **831** (2016) 18-23.

[3] ATLAS collaboration, *Technical Design Report: A High-Granularity Timing Detector for the ATLAS Phase-II Upgrade*, Tech. Rep. CERN-LHCC-2020-007, CERN, Geneva (2020).

[4] CMS collaboration, *A MIP Timing Detector for the CMS Phase-2 Upgrade*, Tech. Rep. CERN-LHCC-2019-003, CERN, Geneva (2019).

[5] C. Li, X. Yang, J. Ge, et al., *Performance of LGAD Sensors with Carbon Enriched Gain Layer Produced by USTC*, *Nucl. Instrum. Methods A* **1039** (2022) 167008.

[6] X. Yang, K. Ma, X. Zheng, et al., *Radiation hardness characterization of low gain avalanche detector prototypes for the high granularity timing detector*, *JUSTC*, **2022** 52(1): 3.

[7] Z. Galloway, C. Gee, S. Mazza, et al., *Use of "LGAD" Ultra-fast Silicon Detectors for Time-resolved Low-keV X-ray Science*, *Nucl. Instrum. Methods A* **923** (2019) 5-7.

[8] S.M. Mazza, G. Saito, Y. Zhao, et al., *Synchrotron Light Source X-ray Detection with Low-Gain Avalanche Diodes*, 2023 *JINST* **18** P10006.

[9] G. T. Saito, M. Leite, S. M. Mazza, et al., *Time-resolved synchrotron light source X-ray detection with Low-Gain Avalanche Diodes*, *Nucl. Instrum. Methods A* **1064** (2024) 169454.

[10] A. Molnar, M. Davis, G. Oregan, et al., *Synchrotron Light Source Focused X-ray Detection with LGADs, AC-LGADs and TI-LGADs*, 2025 *JINST* **20** C07044.

[11] Shanghai Synchrotron Radiation Facility, https://e-ssrf.sari.ac.cn/.

[12] J. He, M. Liu, C. Yin, et al., *Experimental Studies on the X-ray Single-pulse Jitter at the SSRF*, *Nucl. Instrum. Methods A* **1025** (2022) 166038.

[13] *TCAD Sentaurus*, https://www.synopsys.com/silicon/tcad.html.

[14] S. Spannagel, K. Wolters, D. Hynds, et al., *Allpix^2: A modular simulation framework for silicon detectors*, *Nucl. Instrum. Methods A* **901** (2018) 164-172.

[15] X.Yang, *Measurement of VH(H→WW*) process in ATLAS and development of radiation hard LGAD*, CERN-THESIS-2023-157, Sep. 18, 2023.

[16] J.J.Ge, C.H.Li, D.Zhang, et al., *An ultra-fast low-noise preamplifier for Low Gain Avalanche Detectors*, *Nucl. Instrum. Methods A* **1040** (2022) 167222.

[17] SSRF BL16B1, https://e-ssrf.sari.ac.cn/beamlines_2024/sr_72267/beamline_maps/bl16b1/.

[18] A. M. Sirunyan, A. Tumasyan, W. Adam, et al., *Reconstruction of signal amplitudes in the CMS electromagnetic calorimeter in the presence of overlapping proton-proton interactions*, 2020 *JINST* **15** P10002.

[19] J.Z. Zhang, H.Y. Wu, W. Jiang, et al., *Development of a pile-up pulse recovery algorithm for the* $LaBr_3$ *detector*, *Nucl. Instrum. Methods A* **1063** (2024) 169273.

[20] Y. Pawitan, *In All Likelihood: Statistical Modelling and Inference Using Likelihood*, Oxford, 2001; online edn, Oxford Academic, 31 Oct. 2023.

[21] S. S. Wilks, *The Large-Sample Distribution of the Likelihood Ratio for Testing Composite Hypotheses*, *Ann. Math. Statist.* 9 (1) 60 - 62, March, 1938.